CORE
Provided by KITopen
Metadata, citation and similar papers at core.ac.uk

JOURNAL OF SYNCHROTRON RADIATION

ISSN 1600-5775

Received 6 January 2016
Accepted 24 March 2016

Edited by V. Favre-Nicolin, CEA and Université Joseph Fourier, France

Keywords: X-ray diffraction; strain; electro-ceramics; piezoelectrics; ferroelectrics.

Supporting information: this article has supporting information at journals.iucr.org/s

A sample cell for *in situ* electric-field-dependent structural characterization and macroscopic strain measurements

Mohammad J. Hossain,[a] Lijun Wang,[a] Zhiyang Wang,[a,b] Neamul H. Khansur,[a] Manuel Hinterstein,[a,c] Justin A. Kimpton[b] and John E. Daniels[a]*

[a]School of Materials Science and Engineering, UNSW Australia, Sydney, NSW 2052, Australia, [b]Australian Synchrotron, 800 Blackburn Road, Clayton, VIC 3168, Australia, and [c]Institute for Applied Materials, Karlsruhe Institute for Technology, PO Box 3640, 76021 Karlsruhe, Germany. *Correspondence e-mail: j.daniels@unsw.edu.au

When studying electro-mechanical materials, observing the structural changes during the actuation process is necessary for gaining a complete picture of the structure–property relationship as certain mechanisms may be meta-stable during actuation. *In situ* diffraction methods offer a powerful and direct means of quantifying the structural contributions to the macroscopic strain of these materials. Here, a sample cell is demonstrated capable of measuring the structural variations of electro-mechanical materials under applied electric potentials up to 10 kV. The cell is designed for use with X-ray scattering techniques in reflection geometry, while simultaneously collecting macroscopic strain data using a linear displacement sensor. The results show that the macroscopic strain measured using the cell can be directly correlated with the microscopic response of the material obtained from diffraction data. The capabilities of the cell have been successfully demonstrated at the Powder Diffraction beamline of the Australian Synchrotron and the potential implementation of this cell with laboratory X-ray diffraction instrumentation is also discussed.

1. Introduction

Piezoelectric materials generate an electric charge in response to applied mechanical stress (direct effect) and experience a mechanical strain in the presence of an electric field (converse effect). The direct piezoelectric effect is used in sensor or energy harvesting applications and the converse piezoelectric effect is used in actuators such as those used in ultrasound imaging devices. The structural origin of macroscopic piezoelectricity has been the topic of intense investigation over many decades. The electric-field-induced macroscopic strain in piezoelectric materials has been shown to originate from three possible contributions: (i) intrinsic piezoelectric lattice strain, (ii) extrinsic non-180° domain switching and (iii) induced phase transformations (Pramanick *et al.*, 2011; Simons *et al.*, 2013; Hinterstein *et al.*, 2015). X-ray diffraction (XRD) analysis is a very useful tool to observe each of these underlying electro-mechanical coupling mechanisms in piezoelectric materials. The intrinsic strain component can be calculated from diffraction peak position shifts and the extrinsic strain caused by non-180° domain wall motion or phase transformations is quantified from diffraction peak relative intensity changes and splitting and/or broadening of symmetry-dependent reflections. Some fraction of these structural processes can be time-dependent and reversible during actuation. They can range over many orders of magnitude in time, from

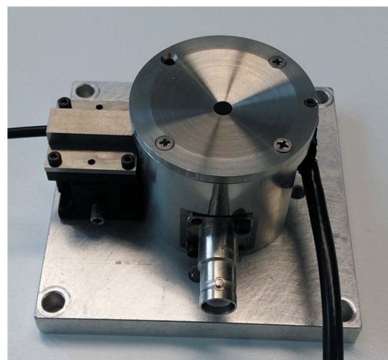

© 2016 International Union of Crystallography

milliseconds to several minutes (Jones *et al.*, 2006; Daniels *et al.*, 2007, 2009, 2014; Hinterstein *et al.*, 2014; Choe *et al.*, 2015). Thus to have a full understanding of the functional mechanisms in these materials, it is necessary to measure diffraction patterns during the application of a field.

In the past, research on functional materials has benefitted from the development of bulk-sensitive *in situ* high-energy (>60 keV) X-ray scattering in transmission geometry (Daniels *et al.*, 2009) and *in situ* neutron scattering (Jones *et al.*, 2006; Daniels *et al.*, 2007; Jones *et al.*, 2007; Zuo *et al.*, 2008; Seshadri *et al.*, 2013). These probes provide several experimental advantages: (i) millimetre-sized samples can be used in conjunction with complex sample environments with little absorption, (ii) sample displacements during actuation have negligible impact on the results observed and (iii) using large area detectors, full strain and texture information can be collected rapidly. However, each of these methods has disadvantages. For high-energy synchrotron X-rays: (i) access to these sources is limited due to the small number of synchrotron beamlines optimized in this energy band, and (ii) optical setups at these beamlines are often optimized for rapid data acquisition, not high resolution, which causes difficulties in observing very subtle structural changes under field. For neutrons, the sample size required for reasonable acquisition times is large (normally on the cm^3 scale), creating difficulties in the material fabrication and increased probability of sample failure under high electric fields. Conventional structural characterization of piezoceramics using low-energy X-ray sources has potential advantages, but presents challenges for *in situ* sample cell design. At lower X-ray energies, diffraction studies of polycrystalline piezoelectric materials are restricted to reflection geometry owing to the generally high absorption coefficients of the materials of interest.

In situ studies in reflection geometry using laboratory-based X-ray instruments and synchrotron X-ray sources have been conducted previously (Pramanick & Jones, 2009; Liu *et al.*, 2005; Li *et al.*, 2002; Kungl *et al.*, 2007; Sakata *et al.*, 2010; Do *et al.*, 2008; Thery *et al.*, 2015; Schmidt *et al.*, 2009). In these scattering experiments, care must be taken to ensure that the sample surface displacement induced by the field is not influencing the measured strain values. If an applied electric field causes the sample surface to displace relative to the X-ray source and detector positions, a pseudo-strain will result, which needs to be carefully accounted for when interpreting the data. Pramanick & Jones (2009) reported a sample surface movement of 4 µm for a 1 mm-thick sample during the application of an electric field. Therefore, owing to this surface movement they found an 18% error in the measured lattice strains, much larger than the typical angular resolution of a powder diffraction instrument.

An additional difficulty for all *in situ* diffraction measurements is that the structural strain mechanisms of piezoelectric materials are often correlated to the measured macroscopic strain collected *ex situ*. Thus, correlating the underlying mechanism to the macroscopic response directly is difficult to achieve. This can be overcome by incorporating a strain sensor into the *in situ* measurement cell.

Here, we demonstrate an electric field sample cell that can overcome these primary difficulties by having a fixed position of the scattering surface in addition to an *in situ* macroscopic strain sensor. The applicability of this newly developed cell has been demonstrated by the electric-field-dependent measurements of commercial soft $PbZr_xTi_{1-x}O_3$ (PZT) and lead-free $0.95(Bi_{1/2}Na_{1/2})TiO_3$–$0.05BaTiO_3$ (BNT-5BT) ceramics at the Powder Diffraction beamline of the Australian Synchrotron (Wallwork *et al.*, 2007). Results show that the developed sample cell offers a new capability to directly correlate the microscopic structural changes observed by XRD with the macroscopic response of electro-mechanical materials under the applied electric field.

2. Experimental procedure

2.1. Sample cell design

Design considerations for the development of an *in situ* sample cell for the application of electric fields to ceramic materials in reflection geometry XRD are: (i) the X-ray scattering surface of sample needs to be static with respect to the X-ray source and detector positions during the application of electric fields, (ii) the total thickness of the cell must be kept small for versatility to mount on different X-ray diffraction instruments, (iii) minimum shadowing of the detector arc, (iv) isolation of high voltage (HV) for safety of users and avoiding equipment damage and (v) built-in strain sensor enabling the concurrent macroscopic strain measurement in the diffraction experiment.

The resulting sample cell design which satisfies the above criteria is shown in Fig. 1. The sample stage is connected to the HV amplifier *via* the HV connector. The outer wall is connected to the ground and the inner insulation (Machinable Glass Ceramic, Macor) is sufficiently dimensioned to guarantee no electrical breakdown occurs. The high-voltage wire connects to a spring through the spring stage, which presses the sample against the lid, maintaining electrical connection to the HV amplifier and thus sustaining the electric field at all times. This design allows the sample to freely expand without moving with respect to the incident beam or detector. At the same time, the integrated displacement sensor monitors the field-induced macroscopic strain, which can later be directly correlated to the structural measurements. The conical opening angle of the lid with an angular range from 10° to 170° allows observations over a broad range of sample orientations, facilitating the alignment of the electric field direction with respect to the incident beam at the desired angle. At 44 mm in height and base plate dimensions of 80 mm × 90 mm and a total weight of 0.63 kg, the sample stage offers a high versatility for a broad range of synchrotron as well as laboratory X-ray instruments.

The strain sensor used is a fibre optical displacement sensor (type D, reflectance dependent, Model D12-C6ET3T5, Serial No. 2719, Philtec, Inc.). The displacement sensor operates in reflection mode with the back surface of the sample stage. During the actuation process the sample expands or contracts

and thus the distance between the sensor tip and the back surface of the sample stage will change, resulting in a measurable strain value. This strain sensor can be used to measure the macroscopic strain up to frequencies of 20 kHz; however, the cell spring assembly will have limitations estimated to be in the 100s of Hz.

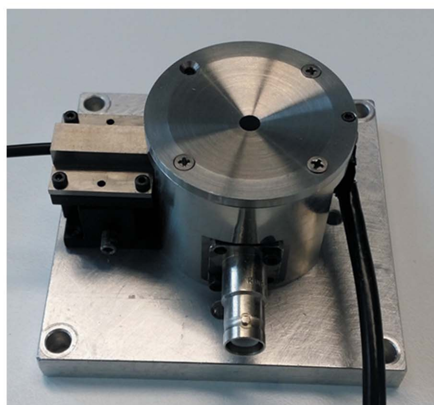

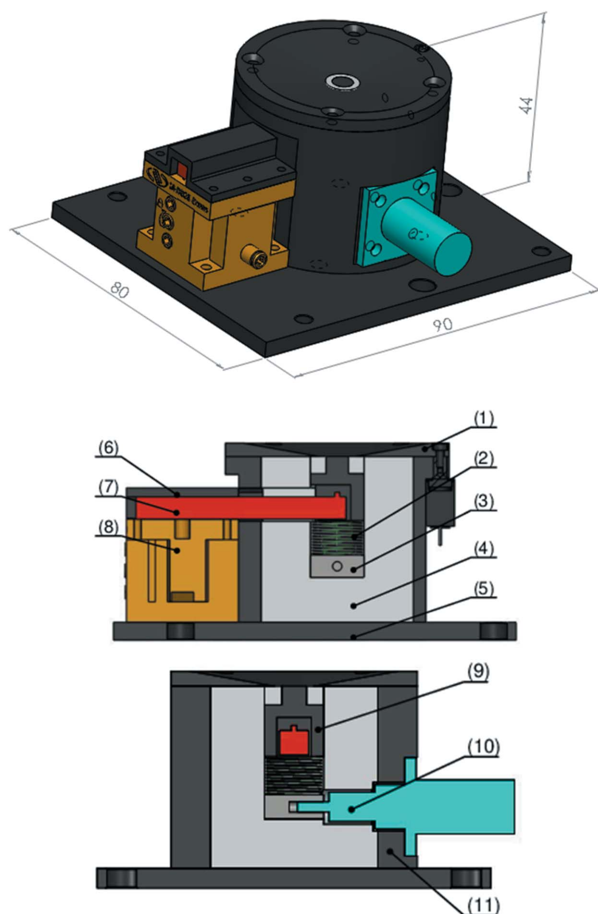

Figure 1
Photograph and schematic drawing of the *in situ* sample cell showing its major components. Lid (1), spring (2), spring stage (3), inner insulating wall (4), base plate (5), displacement sensor bracket (6), displacement sensor (7), linear stage (8), sample mount (9), HV connector (10), outer wall (11).

2.2. Sample preparation

Two types of samples including a soft PZT ceramic (PIC151) and a rhombohedral BNT-5BT lead-free material were used to demonstrate the capabilities of the sample cell. The PZT ceramic sample is commercially available (PI Ceramic, Lederhose, Germany) and the BNT-5BT sample was prepared by a solid-state synthesis route. The BNT-5BT sample was sintered at 1403 K for 3 h in air atmosphere with heating and cooling temperature ramps of 5 K min^{-1}. Further details of the synthesis route are given by Jo & Rödel (2011). Disc-shaped samples suitable for the measurements within the cell were prepared by cutting and polishing to the final dimensions of 8 mm diameter and 1 mm thickness. Prior to the measurements, samples were annealed at 673 K for 30 min to remove any potential residual stresses from the cutting and polishing processes. The top surface of the samples was sputtered with a gold thin film with a thickness of approximately 45 nm. It is thick enough to ensure electric contact and thin enough for ensuring a good penetration of the X-ray beam ($\sim$12 keV energy used here) into the sample. The bottom surface of the samples was coated with a silver paint electrode.

2.3. *In situ* experiment

In situ X-ray scattering experiments were carried out at the Powder Diffraction beamline of the Australian Synchrotron. A monochromatic X-ray beam energy of approximately 12.4 keV (wavelength 0.1 nm) with resolution ΔE = 1×10^{-5} keV was selected by an Si (111) flat crystal pair monochromator. A one-dimensional silicon microstrip-based detector Mythen (Schmitt *et al.*, 2003; Bergamaschi *et al.*, 2010) was used to collect the diffraction patterns with intrinsic angular resolution of 0.004°, covering a 2θ range of 80° and readout time of 250 μs. The experimental setup is shown schematically in Fig. 2. The electric field was generated using a function generator (Agilent 33220 A) and input to the HV power supply (Trek 10/10B-HS). The data acquisition system

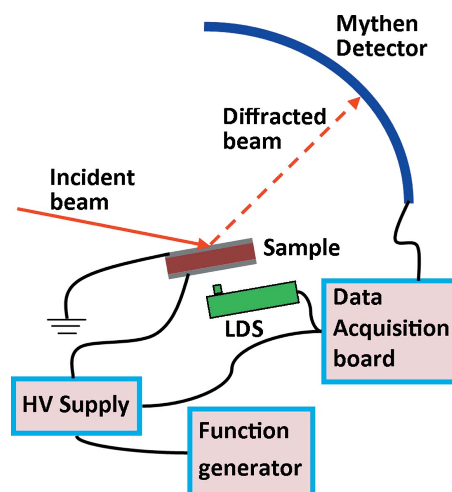

Figure 2
Schematic diagram of the experimental setup with the sample cell used at the Powder Diffraction beamline of the Australian Synchrotron.

recorded the measured output of the displacement sensor and output voltage of the HV power supply. XRD data were collected in reflection geometry using the Mythen detector during the application of bi-polar electric fields with maximum field amplitude of 4.5 kV mm^{-1} in steps of 0.45 kV mm^{-1}. The diffraction data were acquired in a snapshot mode at each field step. In our experimental setup the electric field direction is always perpendicular to the sample surface. In this geometry of the measurement, the incident angle of the X-ray beam is adjusted by tilting the sample stage to make it equal to half of the Bragg angle of the recorded characteristic reflections. During the measurements the electric field vector was aligned approximately perpendicular to the 111 or 200 lattice planes. In the case of PZT, the incident X-ray beam angle was 13.3°, whereas for BNT-5BT was 13.75°.

Suitable profile shape functions were used to fit individual peaks to extract diffraction peak position, area and width using software *Igor Pro 6.37*. Fitted peak positions were used to calculate the material lattice strain.

2.4. Calibration of strain sensor

A soft PZT material (PIC 151) was used as a standard to calibrate the displacement sensor. The reproducible strain response of PIC 151 was used to correlate the measured voltages with a macroscopic displacement of the reflective strain sensor target surface. A unipolar triangular electric field waveform with a maximum field amplitude of 2 kV mm^{-1} and a frequency of 1 Hz was applied. The macroscopic displacement–electric field curves were recorded using a calibrated macroscopic strain measurement system (TF Analyzer 2000 system; aixACCT Systems GmbH, Aachen, Germany). The samples were then mounted in the *in situ* X-ray cell and the distance between the sensor and the target surface was adjusted to set the initial output gain voltage in the centre of the output range of the strain sensor. Electric fields were applied to the sample and the sensor output voltage was recorded simultaneously. Relative movements between the displacement sensor and the target surface were then calculated from the calibrated material strain behaviour. The measured output voltage from the displacement sensor as a function of the gap between the sensor and target surface is plotted in Fig. 3. The gap means the distance between the sensor tip and the target surface (the target surface is the bottom surface of the sample mount shown in Fig. 1). A displacement sensor sensitivity of 36.975 mV µm^{-1} was calculated from the slope of this curve. Such a calibration is required prior to each experimental session, as the reflectivity of the target surface is sensitive to the local environment.

A comparison of the electric field-induced macroscopic strain response in PZT measured using a calibrated strain measurement system and the displacement sensor of the cell during an *in situ* diffraction experiment is shown in Fig. 4(*a*). It can be observed from this figure that the macroscopic strain measured using the cell is in qualitative agreement with that measured using a standard macroscopic strain measurement system. This difference observed here (Fig. 4*a*) is probably due to the difference in cycling conditions for the two experiments. The calibration curve was measured using a continuous

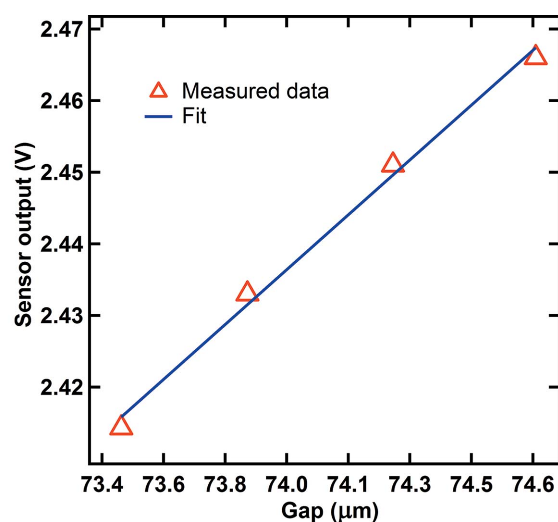

Figure 3
Measured sensor output voltage as a function of the gap between the displacement sensor and the target surface. Red points indicate the measured data and the blue line is the fitted line with a linear approximation. Estimated errors are within the size of the markers.

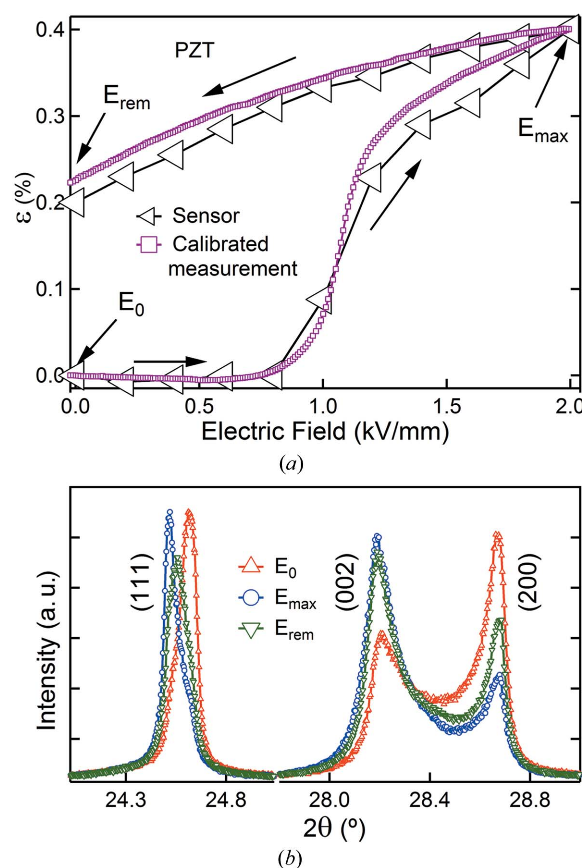

Figure 4
(*a*) Comparison of macroscopic strain curves for PZT measured using a standard strain measurement system (purple line-markers) and the developed sample cell (black line-markers) and (*b*) corresponding *in situ* X-ray diffraction patterns at three electric field states: initial (E_0), maximum (E_{max}) of magnitude of 2 kV mm^{-1} and remnant (E_{rem}) state. Estimated errors are within the size of the markers.

triangular waveform at 1 Hz, whereas the strain data collected from the sample cell were acquired with step-wise field application at a frequency of 0.0011 Hz. Corresponding diffraction patterns at the initial state (E_0), maximum electric field state (E_{max}, 2 kV mm^{-1}) and remnant state (E_{rem}) are shown in Fig. 4(*b*). In the case of PZT, the (111) peak is convoluted with the (111) peak of the gold and cannot be separated. For BNT-5BT, the gold peak position was completely separate, where the (111) peak position of gold was at a 2θ value of 24.545° and the sample was a 2θ value of 25.691°.

3. Results and discussion

Electric field-induced lattice strain (ε_{200}) calculated from X-ray diffraction patterns and simultaneously measured macroscopic strain using the displacement sensor for BNT-5BT are shown in Fig. 5. The lattice strain is approximately 50% of the macroscopic strain at any given field above 1.35 kV mm^{-1}. This is consistent with previous measurements on related materials (Daniels *et al.*, 2007; Pramanick *et al.*, 2009, 2011; Jones *et al.*, 2007) which show in tetragonal and rhombohedral PZTs that the lattice strain is 60% of the measured macroscopic strain during actuation.

Piezoelectric lattice strain is generated on account of local atomic displacements within the unit cell under an external field. Additionally, lattice strain can originate from the

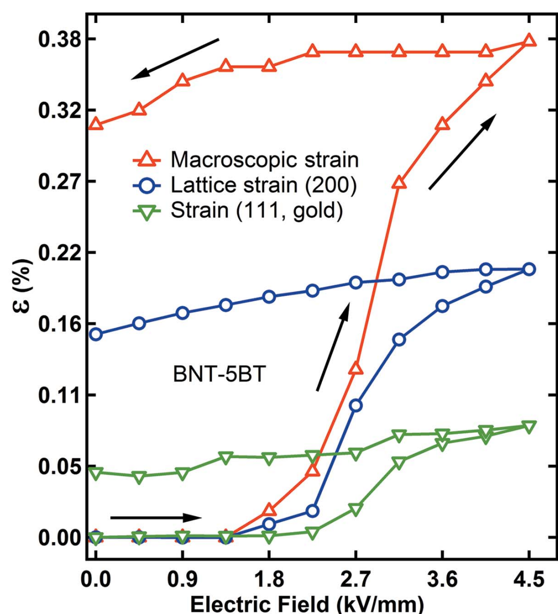

Figure 5
Comparison between the macroscopic strain (red line and markers) measured using a linear displacement sensor and a lattice strain (ε_{200}) (blue line and markers) calculated from X-ray diffraction patterns for BNT-5BT. Data acquisition times for the diffraction data were 45 s per data point. Induced lateral strain (ε_{111}) of gold electrode (green line and markers). The lattice strain was calculated from diffraction peak position shifts during application of the electric field and the macroscopic strains were calculated from the change in the sample dimension parallel to the electric field direction. The lattice strain is approximately 50% of the macroscopic strain at any given field above 1.35 kV mm^{-1}. Estimated errors are within the size of the markers.

compliance of the polycrystalline material with other strain mechanisms in surrounding grains (Pramanick *et al.*, 2011; Hall *et al.*, 2006). The other strain mechanisms are generally extrinsic and are the result of non-180° domain wall motion and/or crystallographic phase transformations (Hinterstein *et al.*, 2015). Macroscopic strain is generated from the combination of total lattice strain and total extrinsic strains generated during the application of an electric field.

One of the crucial features of this cell which allows for accurate *in situ* strain measurements is that the surface of the sample remains static during electric field application. Any movement of the upper surface of the sample will affect the peak position in the diffraction pattern and consequently the calculated lattice strain may be misleading. Here, we have ensured stable conditions by mechanically fixing the diffracting surface of the sample. Therefore, there will be no parasitic movement of the diffracting surface of the sample during the application of an electric field which will affect the strain calculation.

Induced lateral strain of gold on the BNT-5BT surface is shown in Fig. 5. An additional outcome of this constraint is that the gold electrode peaks from the surface could be used to measure the macroscopic d_{31} piezoelectric coefficient of the sample. This is achievable because as the sample expands in the longitudinal direction it contracts in the perpendicular direction. This contraction induces a biaxial stress in the gold electrode which results in a positive lattice strain of the film in the field direction. This response, in the future, could be calibrated for the electrode material, film thickness and diffraction peak used, such that both macroscopic longitudinal d_{33} and transverse d_{31} measurements are made *in situ* with the collection of diffraction data from the sample material.

4. Further considerations

This sample cell can be used in laboratory-based X-ray instruments as well as lower-energy synchrotron sources, where scattering in reflection geometry is used. However, the rate of data acquisition and applied electric field frequency for respective compositions need to be considered for the given instrumentation. For example, the lower intensities of laboratory-based X-ray instruments, where even rapid data collections are on the order of tens of seconds, will prevent experiments where the structural feature of interest changes more rapidly than this.

Careful calibration (Figs. 3 and 4) of the displacement sensor with respect to the reflective target surface and corresponding calibration with the measured values of a standard material is crucial. Any error in the calibration will propagate to the measured strain, yielding erroneous strain results. The error from the calibration will equally reflect in the measured macroscopic strain. For example, if a 1% error exists in the calibration then a 1% error will be in the measured macroscopic strain values also. By direct comparison of the macroscopic strain from the demonstrated cell with that of a calibrated instrument, the error in the calibration is of the order of 1%. Relative to the error in the measured lattice

strains (Fig. 5), this error is approximately the same order of magnitude.

The maximum electrical load of the sample cell is limited by the electrical feedthroughs. Those currently used are capable of 10 kV. However, the real electrical limitation generally arises from the electric field magnitude over the sample thickness (dielectric strength of the material). In previous experiments, the maximum field strength achieved on a range of samples was approximately 5 kV mm^{-1} for samples with silicone grease applied to the outer edges.

Temperature is one of the key factors which changes the phase symmetry and functional properties of electromechanical materials (Jo *et al.*, 2013). Therefore, temperature-dependent property measurements are very important for these materials. Future cell development will concentrate on the addition of a variable temperature option for high- or low-temperature measurements.

5. Conclusions

An electric field sample cell equipped with a macroscopic displacement sensor has been successfully developed and demonstrated to enable the *in situ* structure and macroscopic strain measurements of piezoelectric materials during the application of electric fields. This cell will provide a method to directly probe structure–property relationships in electrically active functional materials and assist in the development of future piezoelectric materials with improved properties.

Acknowledgements

This project was supported by the Australian Research Council (ARC) through Discovery Projects DP120103968, DP130100415 and DE150100750 as well as the BMBF (Bundesministerium fuer Bildung und Forschung) project 05K13VK1. The authors acknowledge the provision of experimental beam time by the Australian Synchrotron.

References

Bergamaschi, A., Cervellino, A., Dinapoli, R., Gozzo, F., Henrich, B., Johnson, I., Kraft, P., Mozzanica, A., Schmitt, B. & Shi, X. (2010). *J. Synchrotron Rad.* **17**, 653–668.

Choe, H., Gorfman, S., Hinterstein, M., Ziolkowski, M., Knapp, M., Heidbrink, S., Vogt, M., Bednarcik, J., Berghäuser, A., Ehrenberg, H. & Pietsch, U. (2015). *J. Appl. Cryst.* **48**, 970–974.

Daniels, J. E., Cozzan, C., Ukritnukun, S., Tutuncu, G., Andrieux, J., Glaum, J., Dosch, C., Jo, W. & Jones, J. L. (2014). *J. Appl. Phys.* **115**, 224104.

Daniels, J. E., Finlayson, T. R., Studer, A. J., Hoffman, M. & Jones, J. L. (2007). *J. Appl. Phys.* **101**, 094104.

Daniels, J. E., Pramanick, A. & Jones, J. L. (2009). *IEEE Trans. Ultrason. Ferroelec. Freq. Control*, **56**, 1539–1545.

Do, D.-H., Grigoriev, A., Kim, D. M., Eom, C.-B., Evans, P. G. & Dufresne, E. M. (2008). *Integr. Ferroelectr.* **101**, 174–181.

Hall, D., Steuwer, A., Cherdhirunkorn, B., Mori, T. & Withers, P. (2006). *Acta Mater.* **54**, 3075–3083.

Hinterstein, M., Hoelzel, M., Rouquette, J., Haines, J., Glaum, J., Kungl, H. & Hoffman, M. (2015). *Acta Mater.* **94**, 319–327.

Hinterstein, M., Rouquette, J., Haines, J., Papet, P., Glaum, J., Knapp, M., Eckert, J. & Hoffman, M. (2014). *Phys. Rev. B*, **90**, 094113.

Jo, W., Daniels, J., Damjanovic, D., Kleemann, W. & Rödel, J. (2013). *Appl. Phys. Lett.* **102**, 192903.

Jo, W. & Rödel, J. (2011). *Appl. Phys. Lett.* **99**, 042901.

Jones, J. L., Hoffman, M., Daniels, J. E. & Studer, A. J. (2006). *Appl. Phys. Lett.* **89**, 092901.

Jones, J. L., Pramanick, A., Nino, J. C., Maziar Motahari, S., Üstündag, E., Daymond, M. R. & Oliver, E. C. (2007). *Appl. Phys. Lett.* **90**, 172909.

Kungl, H., Theissmann, R., Knapp, M., Baehtz, C., Fuess, H., Wagner, S., Fett, T. & Hoffmann, M. J. (2007). *Acta Mater.* **55**, 1849–1861.

Li, X., Shih, W. Y., Vartuli, J. S., Milius, D. L., Aksay, I. A. & Shih, W.-H. (2002). *J. Am. Ceram. Soc.* **85**, 844–850.

Liu, M., Hsia, K. J. & Sardela, M. R. (2005). *J. Am. Ceram. Soc.* **88**, 210–215.

Pramanick, A., Damjanovic, D., Daniels, J. E., Nino, J. C. & Jones, J. L. (2011). *J. Am. Ceram. Soc.* **94**, 293–309.

Pramanick, A., Daniels, J. E. & Jones, J. L. (2009). *J. Am. Ceram. Soc.* **92**, 2300–2310.

Pramanick, A. & Jones, J. (2009). *IEEE Trans. Ultrason. Ferroelec. Freq. Control*, **56**, 1546–1554.

Sakata, O., Yasui, S., Yamada, T., Yabashi, M., Kimura, S., Funakubo, H., Garrett, R., Gentle, I., Nugent, K. & Wilkins, S. (2010). *AIP Conf. Proc.* **1234**, 151–154.

Schmidt, O., Gorfman, S., Bohatý, L., Neumann, E., Engelen, B. & Pietsch, U. (2009). *Acta Cryst.* A**65**, 267–275.

Schmitt, B., Brönnimann, C., Eikenberry, E. F., Gozzo, F., Hörmann, C., Horisberger, R. & Patterson, B. (2003). *Nucl. Instrum. Methods Phys. Res. A*, **501**, 267–272.

Seshadri, S. B., Prewitt, A. D., Studer, A. J., Damjanovic, D. & Jones, J. L. (2013). *Appl. Phys. Lett.* **102**, 042911.

Simons, H., Daniels, J. E., Glaum, J., Studer, A. J., Jones, J. L. & Hoffman, M. (2013). *Appl. Phys. Lett.* **102**, 062902.

Thery, V., Bayart, A., Blach, J.-F., Roussel, P. & Saitzek, S. (2015). *Appl. Surf. Sci.* **351**, 480–486.

Wallwork, K. S., Kennedy, B. J. & Wang, D. (2007). *AIP Conf. Proc.* **879**, 879–882.

Zuo, R., Ye, C., Fang, X. & Li, J. (2008). *J. Eur. Ceram. Soc.* **28**, 871–877.